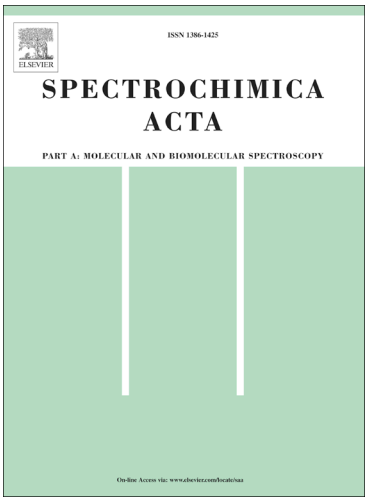

Transient electronic and vibrational signatures during reversible photoswitching of a cyanobacteriochrome photoreceptor

Sean R. Tachibana, Longteng Tang, Cheng Chen, Liangdong Zhu, Yuka Takeda, Keiji Fushimi, Travis K. Seevers, Rei Narikawa, Moritoshi Sato, Chong Fang

PII: S1386-1425(20)31358-5
DOI: https://doi.org/10.1016/j.saa.2020.119379
Reference: SAA 119379

To appear in: *Spectrochimica Acta Part A: Molecular and Biomolecular Spectroscopy*

Received Date: 29 September 2020
Revised Date: 12 December 2020
Accepted Date: 19 December 2020

Please cite this article as: S.R. Tachibana, L. Tang, C. Chen, L. Zhu, Y. Takeda, K. Fushimi, T.K. Seevers, R. Narikawa, M. Sato, C. Fang, Transient electronic and vibrational signatures during reversible photoswitching of a cyanobacteriochrome photoreceptor, *Spectrochimica Acta Part A: Molecular and Biomolecular Spectroscopy* (2020), doi: https://doi.org/10.1016/j.saa.2020.119379

Invited Article for Spectrochim. Acta A (2020) – revised

Transient electronic and vibrational signatures during reversible photoswitching of a cyanobacteriochrome photoreceptor

Sean R. Tachibana [a], Longteng Tang [a], Cheng Chen [a], Liangdong Zhu [a], Yuka Takeda [b], Keiji Fushimi [b], Travis K. Seevers [a], Rei Narikawa [b,d], Moritoshi Sato [c,d], Chong Fang [a,*]

[a] Department of Chemistry, Oregon State University, 153 Gilbert Hall, Corvallis, Oregon 97331-4003, United States

[b] Graduate School of Integrated Science and Technology, Shizuoka University, 422-8529 Shizuoka, Japan

[c] Graduate School of Arts and Sciences, University of Tokyo, 153-8902 Tokyo, Japan

[d] Core Research for Evolutional Science and Technology (CREST), Japan Science and Technology Agency, 332-0012 Saitama, Japan

*To whom correspondence should be addressed. Email: Chong.Fang@oregonstate.edu

Keywords: Cyanobacteriochromes, photoconversion, time-resolved laser spectroscopy, excited-state reaction coordinate, protein cofactor structural dynamics, femtosecond stimulated Raman

Abstract

Cyanobacteriochromes (CBCRs) are an emerging class of photoreceptors that are distant relatives of the phytochromes family. Unlike phytochromes, CBCRs have gained popularity in optogenetics due to their highly diverse spectral properties spanning the UV to near-IR region and only needing a single compact binding domain. AnPixJg2 is a CBCR that can reversibly photoswitch between its red-absorbing ($^{15Z}P_r$) and green-absorbing ($^{15E}P_g$) forms of the phycocyanobilin (PCB) cofactor. To reveal primary events of photoconversion, we implemented femtosecond transient absorption spectroscopy with a homemade LED box and a miniature peristaltic pump flow cell to track transient electronic responses of the photoexcited AnPixJg2 on molecular time scales. The 525 nm laser-induced P_g-to-P_r reverse conversion exhibits a ~3 ps excited-state lifetime before reaching the conical intersection (CI) and undergoing further relaxation on the 30 ps time scale to generate a long-lived Lumi-G ground state intermediate en route to P_r. The 650 nm laser-induced P_r-to-P_g forward conversion is less efficient than reverse conversion, showing a longer-lived excited state which requires two steps with ~13 and 217 ps time constants to enter the CI region. Furthermore, using a tunable ps Raman pump with broadband Raman probe on both the Stokes and anti-Stokes sides, we collected the pre-resonance ground-state femtosecond stimulated Raman spectroscopy (GS-FSRS) data with mode assignments aided by quantum calculations. Key vibrational marker bands at ~850, 1050, 1615, and 1649 cm^{-1} of the P_r conformer exhibit a notable blueshift to those of the P_g conformer inside AnPixJg2, reflecting the PCB chromophore terminal D (major) and A (minor) ring twist along the primary photoswitching reaction coordinate. This integrated ultrafast spectroscopy and computational platform has the potential to elucidate photochemistry and photophysics of more CBCRs and photoactive proteins in general, providing the highly desirable mechanistic insights to facilitate the rational design of functional molecular sensors and devices.

1. Introduction

Photosensing proteins allow living organisms to detect light and convert incident photons into a biochemical response [1]. Almost all proteins can absorb light in the UV region due to the presence of aromatic amino acids such as tyrosine, tryptophan, or phenylalanine, but the ability to detect visible to near-IR light is desirable for bioimaging [2-4] and optogenetic applications [5-8]. Besides the photoreceptors found in the eyes of animals, phytochromes and cyanobacteriochromes (CBCRs) are the best known visible light receptors [9-11]. Phytochromes share the conserved PAS (Per/ARNT/Sim), GAF (cGMP-phosphodiesterase/adenylate cyclase/formate hydrogen lyase transcription activator FhlA), and PHY (phytochrome-specific) domains, wherein the GAF domain is responsible for covalently binding a linear tetrapyrrole (bilin) chromophore that is necessary for light detection [1]. The PAS-GAF-PHY architecture is required for a functional photocycle in canonical phytochromes. In contrast, CBCRs only require the GAF domain for proper chromophore binding and photoconversion (e.g., regulating the phototaxis of cells), which allows for a more desirable size for application purposes. Some of the most common bilin chromophores are phycocyanobilin (PCB, found in algae and cyanobacteria), phytochromobilin (PΦB, found in plants), and biliverdin IXα (BV, a mammalian-intrinsic chromophore) that allow this superfamily to obtain a diverse spectral property from the UV to near-IR region. Upon photoexcitation, these photosensors undergo a Z/E isomerization at the C15=C16 bond (by the D-ring) of the cofactor chromophore (Fig. 1b) [9,12]. As these photosensors undergo the light-induced conversion, they adopt a Lumi-intermediate state where the chromophore resides in a twisted conformational state but the overall protein has not fully relaxed to establish the new chromophore environment.

In the phytochrome and CBCR family, many proteins share similar chromophores and GAF domains, yet they are able to display different spectral properties and dynamics. Previous studies

of a popular cyanobacterial phytochrome, Cph1, have reported the ultrafast dynamics for P_r/P_{fr} (red/far-red) photoconversion [9,13,14]. Dasgupta et al. reported a major 3 ps time constant responsible for the initial Z-to-E isomerization at the C15=C16 bond of the bilin prosthetic group [9]. The isomerization leads to production of Lumi-R* (the asterisk indicates the electronic excited state) population that decays to the Lumi-R ground state on the ~30 ps time scale. A closely related CBCR, NpR6012g4, was studied by Kim et al. via ultrafast spectroscopy of both photoconversion ($P_g \leftrightarrow P_r$) processes [15,16], invoking heterogeneous ground-state populations that photoconvert on different time scales. Overall, the forward ($^{15Z}P_r$ to $^{15E}P_g$) photoconversion exhibits a longer excited-state lifetime and reaches the conical intersection (CI) after ~75 ps to 1 ns. The reverse ($^{15E}P_g$ to $^{15Z}P_r$) photoconversion shows a shorter excited-state lifetime and reaches the CI after ~2 ps. When comparing the photoconversion of P_r to P_g in CBCR with P_r to P_{fr} in Cph1, they share the same cofactor 15Z-to-15E isomerization but differ in the hypso/bathochromic shift, quantum yield (see Section 3.3 below), and change of LUMO energy. For the P_r-to-P_g transition, the LUMO is destabilized whereas the P_r-to-P_{fr} photosensors show a stabilized LUMO [17].

In this work, we investigated one of the first described hypsochromic red/green CBCR GAF2 protein encoded from Anabaena sp. PCC7120 (AnPixJg2) [18,19]. Under ambient light, AnPixJg2 adopts a mix of red light-absorbing ($^{15Z}P_r$) and green light-absorbing ($^{15E}P_g$) species, with the superscripts highlighting the photoinduced Z/E isomerization of a key double bond (C15=C16, Fig. 1b) adjacent to the most flexible D-ring of the chromophore (i.e., between the 15Z isomer at the resting "red" state and the 15E isomer at the photoproduct "green" state). By exciting AnPixJg2 with red or green light, the protein photoconverts to the P_g and P_r states in a reversible manner. Although AnPixJg2 has its size advantage over the bulkier phytochromes, AnPixJg2 utilizes PCB as its chromophore which is biologically unavailable in mammalian cells. In addition, AnPixJg3

(GAF3) is photo-inactive whereas AnPixJg4 (GAF4) shows P_r-to-P_g photoconversion and rapid P_g-to-P_r dark reversion [8,18]. Therefore, mechanistic insights into the structure and dynamics of key residues, which play important roles for photoconversion, would enable protein engineers to identify photoactive GAF domains through amino acid sequencing, site-specific mutagenesis, and targeted evolution. Previous nanosecond studies on AnPixJ has provided information of four intermediates formed on the nanosecond to millisecond time scales [20], but deeper insights into the primary photodynamic events on even shorter time scales would allow for a fuller picture of photoconversion that leads to function. To help remedy these shortcomings with fundamental understanding, we have implemented a series of studies, first of which utilized femtosecond transient absorption (fs-TA) and global analysis, followed by the wavelength-tunable ground-state femtosecond stimulated Raman spectroscopy (GS-FSRS) and quantum calculations to delineate the ultrafast dynamics of both photoswitching processes between P_r and P_g states of AnPixJg2.

2. Experimental materials and methods

2.1. Protein sample preparation

Protein expression. The His-tagged AnPixJg2 (amino acid positions 221–397) and AnPixJg2_BV4 inserted into pET28a vector (Novagen) have been constructed in the previous studies [18,21]. These plasmids were transferred into the Escherichia coli strain C41 (Cosmo Bio) harboring phycocyanobilin (PCB) synthetic system (pKT271-C0185) or biliverdin (BV) synthetic system (pKT270) for protein expression [22,23]. The bacterial cells were grown on Lysogeny Broth (LB) agar medium at 37 °C and selected by kanamycin and chloramphenicol (each final concentration, 20 μg mL^{-1}). The selected cells were cultured in 1 L LB medium at 37 °C until the cell optical density at 600 nm was reached at 0.4–0.8. Subsequently, isopropyl β-D-1-

thiogalactopyranoside (final concentration, 0.1 mM) was added into the culture media and these cells were cultured at 18 °C overnight to induce the protein expression.

Protein extraction and purification. After protein expression was induced, the culture broth was centrifuged at 5,000 g for 15 min to collect cells and then frozen at –80 ºC. The cells were suspended in a lysis buffer (20 mM HEPES-NaOH pH=7.5, 0.1 M NaCl, and 10% (w/v) glycerol) and disrupted by Emulsiflex C5 high-pressure homogenizer at 12,000 psi (Avestin, Inc.). The mixtures were centrifuged at 165,000 g for 30 min to remove pellets. The collected solutions were filtered through a 0.2 μm cellulose acetate membrane. Followed by the addition of imidazole (final concentration, 30 mM), the solution was loaded onto a nickel-affinity His-trap column (GE Healthcare) using an ÄKTAprime plus (GE Healthcare). After washing the column with the lysis buffer containing 30 to 100 mM imidazole, His-tagged proteins were purified using the lysis buffer containing 100 to 400 mM imidazole with a linear gradient system (1 mL/min, total 15 min). The purified proteins were incubated with 1 mM EDTA on ice for 1 h and then dialyzed against the lysis buffer to remove imidazole and EDTA.

2.2. LED box design and flow cell methods

The homemade 3D-printed box measures 10 × 10 × 6 cm^3 (L × W × H) with a 5-mm-diameter hole centered on each side [24]. The sample holder was printed at the box center, ~4 cm away from the LEDs inserted through the holes on four sides. Four Broadcom Limited 5 mm through-hole cyan LEDs centered at 505 nm were used to photoconvert P_g to P_r, operated at 3.2 V and 20 mA per LED. The P_r-to-P_g photoconversion used four VCC 5 mm though-hole red LEDs centered at 650 nm working at 2.1 V and 20 mA per LED. The measured irradiation power of the four 505 nm and 650 nm LEDs at the sample holder is ~3.2 mW and 1.0 mW, respectively. The CBCR sample

was circulated from the LED box to a 1-mm-pathlength quartz flow cell using a Gikfun 12V DC peristaltic pump. A 1 × 2 mm (ID x OD) uxcell silicone tubing was used to keep the total loop volume of ~1.8 mL. AnPixJg2 was kept in its dominant P_r or P_g forms under constant illumination of 505 or 650 nm LEDs, respectively. Fresh P_r or P_g sample solution was continuously flowed into the laser beam path in the optical setup to observe the photoconversion process via time-resolved electronic spectroscopy and collect the associated ground-state vibrational spectra (vide infra).

The flow rate was calculated by measuring the time (83 s) to flow 10 mL sample solution at 0.12 mL/s. Given the flow cell dimension of 0.8 × 0.1 × 4 cm^3 (L × W × H) with a total volume of 0.3 mL (48-Q-1, Starna Cells), the top surface area is 0.08 cm^2, so the distance that solution can flow through the cell per second is 1.5 cm. The diameter of laser focal point at the sample was measured to be ~150 μm (0.015 cm), hence it takes ~10 ms to completely refresh the sample within the entire laser spot. Since each spectral data point was collected in our experiments with 3,000 laser shots (see Section 2.4 below) at 1 kHz repetition rate, recording the signal consecutively in the chopper on and off cycle, there are 5 laser pulses acting as the pump (with the corresponding probe) before the sample solution becomes completely replenished, then repeated for 300 times to increase the signal-to-noise ratio. Though the excited sample solution may have a very small percentage of transient photoswitching products (e.g., Lumi-R or Lumi-G as detailed in Section 3 below) within each five-pump-pulse cycle, while the pump wavelength has a weak overlap with the absorption of the intermediates (Lumi-G or Lumi-R) or final products (P_r or P_g, see Fig. 1a), the reported ultrafast electronic spectra on the femtosecond to nanosecond time scales are not affected and thus accurately reflect the chromophore dynamics under investigation.

2.3. Steady-state electronic spectroscopy

The steady-state absorption spectra of CBCR samples in buffer solution housed in a 1-mm-pathlength quartz cuvette (Spectrosil 1-Q-1, Starna Cells) were collected by a Thermo Scientific Evolution 201 UV/Visible spectrophotometer. The protein sample concentration was set at OD≈1 per mm for the 648 nm absorption peak under ambient conditions (see Figs. 1a and S1). Meanwhile, the steady-state emission spectra of the protein samples in buffer were examined using a Shimadzu RF-6000 spectrofluorophotometer, wherein the arc lamp was also used for the excitation-dependent absorbance measurements (Fig. S2). For each case, the excitation slit width was set to 5.0 nm and a mirror was placed on the back to allow for the excitation light to reflect back and cover the full area of the sample quartz cuvette. Before each data collection, the sample was exposed under ambient light for 5 min to fully convert back to the native state. The sample was then photoexcited for 1 min before promptly collecting the absorption spectrum. All other ambient lights in the lab were turned off to minimize any back photoconversion. All the experiments were performed at room temperature and 1 atm pressure.

In the Narikawa lab, UV/Visible absorption spectra of the newly prepared proteins were recorded with a Shimadzu UV-2600 spectrophotometer at room temperature. Monochromatic light at various wavelengths for inducing photoconversion was generated by an Opto-Spectrum Generator (Hamamatsu Photonics, Inc.): P_g form, at 540 nm; P_r form, at 650 nm (see Fig. S1).

2.4. Femtosecond transient absorption (fs-TA) spectroscopy and femtosecond stimulated Raman spectroscopy (FSRS)

Time-resolved light-induced electronic responses of the CBCR cofactor were collected via a fs-TA setup with ultrafast laser pulses from a Ti:sapphire-based regenerative laser amplifier (Legend-Elite-USP-1K-HE, Coherent, Inc.) seeded by a Ti:sapphire-based oscillator (Mantis-5,

Coherent, Inc.). The fundamental output laser pulse train has a center wavelength of ~800 nm, average power of ~3.70 W, and repetition rate of 1 kHz, which was split up to generate the tunable fs actinic pump (ca. 480–720 nm) for photoexcitation, ps Raman pump (ca. 480–720 nm), and fs supercontinuum white light (SCWL) probe [25,26]. In particular, we used a home-built two-stage noncollinear optical parametric amplifier (NOPA) to generate the 525 and 650 nm actinic pump with ~0.3 mW average power for fs-TA experiments, initiating the $P_g \rightarrow P_r$ and $P_r \rightarrow P_g$ processes, respectively. Temporal compression of the actinic pump was achieved by a chirped mirror pair (DCM-12, 400–700 nm, Laser Quantum, Inc.). The broadband probe beam was created by focusing a small portion of the fundamental laser pulses on a 2-mm-thick quartz cuvette filled with deionized water, followed by temporal compression via a chirped mirror pair (DCM-9, 450–950 nm, Laser Quantum, Inc.). The pump and probe beams were focused on the sample solution in a 1-mm-thick quartz flow cell (see Section 2.2), and the cross-correlation time between the incident fs pump and probe pulses was measured to be ~120 fs in methanol housed in the 1-mm-thick quartz cuvette. A motorized linear translation stage (NRT150, Thorlabs, Inc.) was used to precisely control the time delay up to 900 ps for the preceding actinic pump (versus the probe fixed in time).

Using the aforementioned fs laser amplifier system, the light-induced vibrational responses of the CBCR cofactor were collected via FSRS methodology in the electronic ground state (S_0). The ps Raman pump was generated by a home-built three-stage NOPA system, which consists of one fs-NOPA and spectral filter that produce the ps tunable seed pulse as well as a subsequent two-stage ps-NOPA for intensity amplification, while the ps 400 nm pump pulses were generated by a home-built second harmonic bandwidth compressor (SHBC) of the fs 800 nm fundamental laser pulses [27]. Using a neutral density filter, we set the output ps Raman pump power to ~2 mW at 500, 596, 633, and 678 nm (specific wavelengths used in FSRS experiments). In addition, we

implemented the conventional FSRS setup with a ps, ~2 mW, 792 nm Raman pump to achieve a pre-resonance condition while minimizing spectral overlap with the P_g and P_r absorption bands (hence photoswitching behavior, see Figs. S1 and S2). All the laser pulses were parallel polarized.

In the fs-TA and FSRS setups, a phase-locked optical chopper (Newport 3501) was inserted in the beam path of the actinic pump and Raman pump, respectively. Time zero was set when either pump pulse is coincident with the SCWL probe pulse at the focusing point on the sample cell. The transmitted probe was collimated and focused into an imaging spectrograph (IsoPlane SCT-320, Princeton Instruments, Inc.) with a reflective grating (300 grooves/mm, 300 nm blaze wavelength for TA; 1200 grooves/mm, 500 nm blaze wavelength for FSRS) for dispersed detection and an integrated front-illuminated CCD array camera (PIXIS:100F, Princeton Instruments, Inc.) at the exit plane. To improve the signal-to-noise ratio, we used 3,000 laser shots per point and six sets in fs-TA (hence 9,000 spectra averaged at each time delay point), and 3,000 laser shots per point and 60 sets in FSRS (hence 90,000 spectra averaged for each ground-state Raman spectrum) [28]. To overlay the GS-FSRS spectra collected on the Stokes and anti-Stokes sides for comparison, the Raman intensity and Raman shift axes need to be multiplied by –1 for the latter case [28,29].

2.5. Quantum calculations

The vibrational normal mode frequencies of the PCB cofactor of AnPixJg2 in the electronic ground state (S_0) were calculated in vacuo with density functional theory (DFT) at the RB3LYP level using Gaussian 16 software [30]. The PCB chromophore in P_r form was directly taken from the reported crystal structure of AnPixJg2 (PDB ID:3W2Z) [19]. The two propionate ($–C_2H_4COO^–$) groups on the B and C rings were removed and capped with methyl ($–CH_3$) groups to avoid calculation complexation, while proper numbers of hydrogen atoms were added to the

chemical structure using GaussView 6. The total number of charges is +1 (i.e., a protonated nitrogen site on the C ring). To mimic structural restraints from the PCB local environment in the GAF2-binding pocket, two bridge-dihedral angles between the C and D rings were fixed to their values in the reported crystal structure before optimization. The PCB structure was first optimized with 3-21G basis sets, further optimized with 6-31G, then 6-31G(d,p) basis sets, followed by the vibrational frequency calculation in the resting state (i.e., P_r). Due to the lack of crystal structure with PCB in the P_g state of AnPixJg2, we adopted the P_g crystal structure of Slr1393g3 (PDB ID: 5M82) [31], which is also a red/green CBCR [32] and in close relationship with AnPixJg2 [11]. The PCB chromophore structure therein shows both twisting of the D and A rings. Therefore, the two dihedral angles between A and B rings were also fixed, in addition to the two dihedral angles between C and D rings, before geometric optimization. The P_g molecular structure was then optimized and vibrational frequencies were calculated following the same steps as calculations for the P_r structure to provide an informative comparison between these two conformers. The Raman spectra were exported with 10 cm^{-1} half width at half height (HWHH) and 9 cm^{-1} step size as well as a frequency scaling factor of 0.97 [33,34] to juxtapose with the experimental FSRS spectra collected in the electronic ground state of the respective PCB conformers in AnPixJg2 (vide infra).

3. Results and discussion

3.1. Steady-state and time-resolved electronic spectroscopy

In order to keep AnPixJg2 in the P_r or P_g conformers, a home-built LED box was made that fits four 5 mm through-hole LEDs with a center wavelength of 505 or 650 nm. Approximately 2 mL of AnPixJg2 in buffer was kept at the center of the LED box with an OD of ~1/mm at the P_r absorption peak (~650 nm, see Fig. 1a). The sample was pumped into a flow cell so no LED light

could be scattered into the optical setup for fs-TA and FSRS experiments, while allowing for new fresh sample to be flown in (see Sections 2.2 and 2.3). In fs-TA setup, the photoconversion reaction was initiated using the fs-actinic pump centered at 525 nm (Fig. 1a, green dashed) and 650 nm (Fig. 1a, red dashed) for the $P_g \rightarrow P_r$ and $P_r \rightarrow P_g$ process, respectively. As a control, the sample was placed in the actinic pump beam path before it was focused (to less than 150 μm diameter at the sample spot [35], see Section 2.2) and we observed a clear color change within seconds, indicating that the fs actinic pump pulse train is capable of photoswitching AnPixJg2 between conformers.

Starting from time zero of photoexcitation, the $P_g \rightarrow P_r$ reaction shows three major features at ~690, 620, and 544 nm (Fig. 2a). The negative band around 544 nm is attributed to the ground-state bleaching (GSB) of the photoexcited P_g population that overlaps with the residual scattering from the actinic pump (see Fig. S3a). A probe-dependent fit was taken at the bluer 504 nm (Fig. 2c, blue) to retrieve clearer GSB dynamics without significant influence from the pump scattering at 525 nm and the rising excited-state absorption (ESA) band around 595 nm (tentatively assigned here, see below for details). Since the GSB recovery was tracked on the blue edge with a reduced signal-to-noise ratio (thus hindering an accurate assessment of the long-time recovery percentage on the tens of ps to hundreds of ps time scales), only major dynamic components of ~100 fs and 5 ps were retrieved. The 5 ps time constant is consistent with other reported $^{15E}P_g$-to-$^{15Z}P_r$ conversions in similar CBCRs [16], which is longer than the ca. 1–3 ps observed for the PCB cofactor in Cph1 phytochrome reverse and forward photoconversions [9,14].

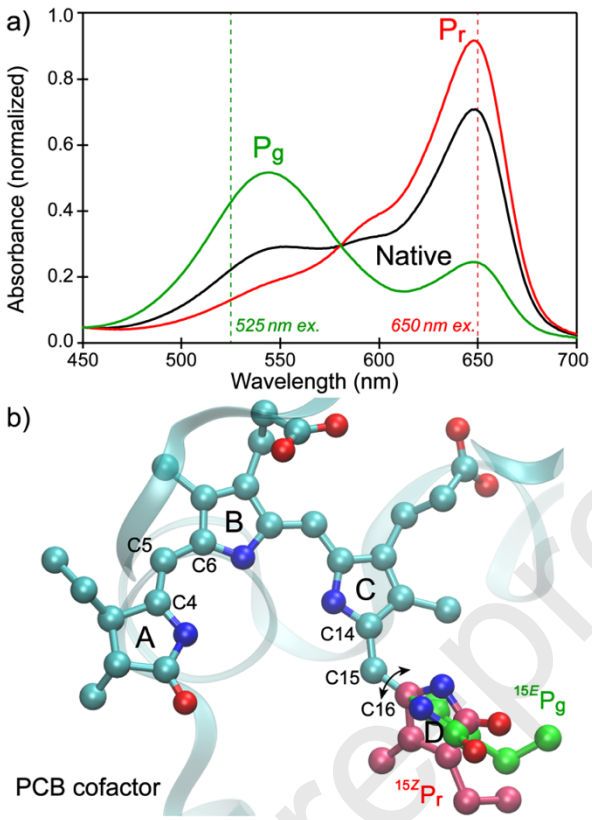

Fig. 1. Steady-state absorption profiles of the AnPixJg2 cofactor. (a) Ground-state electronic absorption spectra of the AnPixJg2-PCB native (black), $^{15Z}P_r$ (red), and $^{15E}P_g$ (green) species normalized at 280 nm, obtained upon 1 min irradiation of ambient white light, 505 nm LEDs, and 650 nm LEDs, respectively. The P_r form has a λ_{max}=648 nm and a shoulder at 592 nm while the P_g form has a λ_{max}=544 nm. The actinic pump wavelengths in TA experiments are noted by dashed lines. (b) Crystal structure of the PCB cofactor in the P_r state (PDB ID: 3W2Z) and illustration of the D-ring twist in the P_g state inside the protein pocket (a model structure based on Slr1393g3, PDB ID: 5M82; see Graphical Abstract for directly overlaid structures). The light-induced $P_r \rightarrow P_g$ switching thus represents a primary photoreaction with Z-to-E isomerization of the chromophore with twisting (black curved arrows, D-ring colored from red to green by ~90º for illustration) around the C15=C16 bridge between the C/D rings. Carbon, nitrogen, and oxygen atoms are shown as cyan, blue, and red spheres, respectively, while hydrogen atoms are omitted for simplicity.

The dominant positive band around 692 nm corresponds to the P_g* ESA (the asterisk denotes the electronic excited state, e.g., the first singlet excited state S_1) most likely from S_1 to S_2 because the band reaches maximum intensity close to time zero and is located on the red edge (i.e., lower energy side of the spectral detection window). Another P_g* feature that starts from time zero is the negative band at ~649 nm, which represents the downward stimulated emission (SE) transition from S_1 to S_0. Both P_g* bands (ESA and SE) decay within tens of ps in the TA contour plot (Fig. 2a) with ~3.5 and 2.8 ps time constants (Fig. 2b, red and Fig. 2c, green) that largely match the P_g GSB recovery component of ~5 ps, supporting a peaked CI that bifurcates into different species [36,37]. This few-ps time scale likely involves local orientational relaxation of the chromophore D-ring and its immediate vicinity. The longer 22 and 32 ps decay components of the P_g* ESA and SE bands are attributed to the relaxation of the photoconverted species after the CI, while the additional ~1.6 ns decay of the P_g* SE band probes the (weak) fluorescence lifetime back to P_g.

The most interesting feature in the photoinduced $P_g \rightarrow P_r$ transition is the rise of a long-lived absorption band around 595 nm. This transient band appears after several ps with the retrieved time constants of ~120 fs (decay), 3.1 ps (rise), 19 ps (rise), and 1 μs (decay) (Fig. 2b, black). The sub-ps component overlaps with the above-mentioned GSB and SE bands, resulting in a gradual signal rise from the negative to positive region. In contrast to the P_g* ESA band at 692 nm that diminishes after ~50 ps, the long-lived characteristic of the 595 nm positive band suggests that it is more likely associated with a ground-state population of Lumi-G. The 1 μs decay time constant was used to estimate the Lumi-G lifetime that extends well beyond our detection time window (see Section 2.4). For corroboration, Fukushima and coworkers identified two metastable ground-state intermediates for the P_g-to-P_r photoconversion within ~50 ns and 190 μs [20]. The 3.1 ps rise component corresponds to the P_g* species moving into the CI, which closely matches the decay of

both the P_g* ESA (3.5 ps) and SE (2.8 ps) as well as the GSB recovery (5 ps). The slight 19 ps rise component could represent further relaxation of Lumi-G that is evident by the noticeable blueshift of the ~600 nm absorption band (Fig. 2a) [38], also in accord with the 22–32 ps time constants retrieved from the P_g* decay dynamics (Fig. 2b,c).

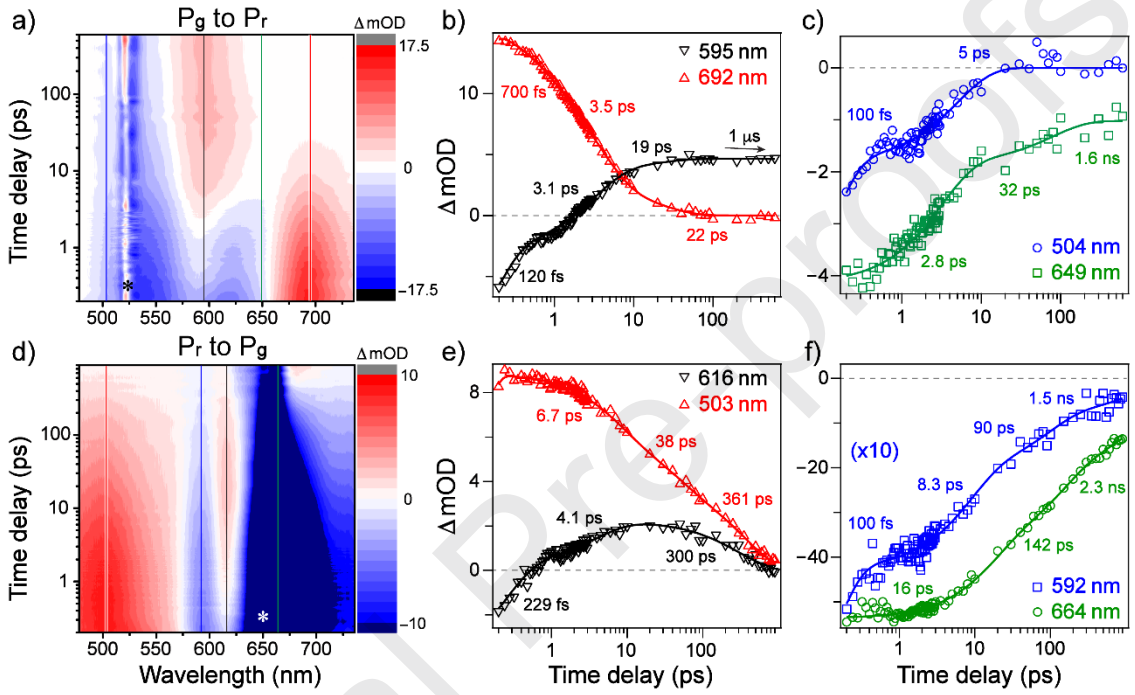

Fig. 2. Time-resolved electronic spectra during reversible photoswitching processes of AnPixJg2. The fs-TA contour plot of (a) $P_g \rightarrow P_r$ and (d) $P_r \rightarrow P_g$ transition was collected using a 525 nm actinic pump with 650 nm LEDs and 650 nm actinic pump with 505 nm LEDs, respectively. Colored vertical lines correspond to the specific spectral region for the probe-dependent least-squares fits (b, c, e, and f). The 592 nm data points and fit (f, blue) are scaled by a factor of 10 for better visual comparison to the much stronger 664 nm data plot (f, green). In both photoswitching cases of the PCB cofactor, scattering from the actinic pump (denoted by the asterisks in panels a and d) was largely removed by subtracting the –2 ps TA trace from the subsequent time-resolved TA traces (raw spectra shown in Fig. S3).

For the $P_r \rightarrow P_g$ conversion, the fs-TA 2D contour plot (Fig. 2d) exhibits a longer P_r* lifetime (than the P_g* lifetime in Fig. 2a) since the initial bands reaching maximum around time zero fully decay away after hundreds of ps. In particular, the prominent P_r* features include the 503 nm ESA and 664 nm SE bands, which exhibit pure decay time constants of ~6.7, 38, and 361 ps (Fig. 2e, red) and ~16 ps, 142 ps, and 2.3 ns (Fig. 2f, green). The 664 nm SE band mainly probes the fluorescence pathway of P_r* back to P_r that was previously reported to be centered at 670 nm [20]. The much weaker, narrow, negative band at 592 nm could be assigned to GSB due to its proximity to a shoulder peak within the P_r ground-state absorption (GSA) band (Fig. 1a). Notably, in contrast to the aforementioned 595 nm absorption band in Fig. 2a, we observed the distinct rise and decay of a narrow 616 nm absorption band in Fig. 2d. The short-lived characteristic is indicative of an excited-state species that we denote as a P_r*' intermediate via continuous structural evolution of the PCB chromophore [39]. The strongly overlapped TA bands hinder a clearer identification of the intermediate state. However, previous QM/MM studies of AnPixJg2 [40] as well as spectroscopic studies on other CBCR and phytochrome systems [9,12,15] suggest that P_r*' could have a deprotonated chromophore in an unrelaxed protein pocket (i.e., as a transient precursor to the intermediate Lumi-R state with a deprotonated PCB chromophore [20]). Further excited-state vibrational studies (e.g., tunable FSRS) are needed to track proton transfer dynamics [25,28] and shed more light on P_r*' (e.g., whether a change of protonation state occurs on the ~10 ps time scale as shown in Fig. 2e,f), though recent work has supported a fully protonated chromophore in both equilibrium forms (i.e., after protein relaxation hosting the isomerized cofactor) [41-43].

By comparing the TA dynamics that emerge from initial photoexcitation, the hundreds of fs time constants (100–229 fs) can only be extracted from the GSB recovery at 592 nm (Fig. 2f, blue) and initial decay at the neighboring still-negative 616 nm band (Fig. 2e, black). The other retrieved

time constants from the highly overlapped bands show a weighted average that could involve multiple steps of P_r* relaxation on the ps-to-ns time scales. The P_r*-to-P_r*' transition occurs on the 6.7–16 ps time scales as these time constants can be correlated with the P_r*' rise component (4.1 ps, Fig. 2e, black). Furthermore, the 361 ps decay component (from the 503 nm ESA band of P_r*, Fig. 2e, red) and 300 ps decay component (from the 616 nm ESA band of P_r*', Fig. 2e, black) represent the excited-state populations that enter the CI for photoconversion. This assignment is supported by previous TA experiments on a similar red/green CBCR, NpR6012g4, where Kim and coworkers found 55 and 345 ps lifetimes that generate the photoproduct Lumi-R state [15]. The GSB recovery dynamics at 592 nm (Fig. 2f, blue) largely match the main GSB decay time constants at 648 nm of ~100 fs, 11 ps, 91 ps, and 1.5 ns. On the red side of the 648 nm GSB band is the 664 nm SE band that overlaps with a weak fluorescence band of P_r (see Fig. S3). Even after subtracting the actinic pump scattering, the 648 nm GSB and 664 nm SE signal (Fig. 2d, dark blue region) was ~10 times larger than other spectral features, therefore the color scale was fixed to better resolve the weaker TA bands. Temporal evolution of these strong negative features in the ca. 625–700 nm region can be better viewed in the raw time-stacked TA spectra (Fig. S3).

To further dissect the overlapped TA spectra and elucidate the underlying reaction species, global analysis can fit the data to a postulated multi-population model to obtain the respective concentration and time constants [44,45]. A series of linear differential equations is used on a target model to be numerically solved and yield the best results. The evolution-associated difference spectra (EADS) implement multiple sequential states to extract time constants from spectral evolution during a reaction; however, it does not directly give the species-specific rate constants that describe the evolution of populations from one to another [44,46]. Decay-associated difference spectra (DADS) describe the data in a parallel model with each species decaying with

a distinct lifetime [47,48]. Using both schemes for the fs-TA spectra of AnPixJg2, the singular value decomposition suggested a four-component model (Fig. 3) that was validated by having more components that only fit the early-time coherent artifacts or fewer components that lead to averaged longer time constants. In general, the sequential reaction model should work well here as a stepwise isomerization mechanism was proposed in related red/green CBCR systems [12,20].

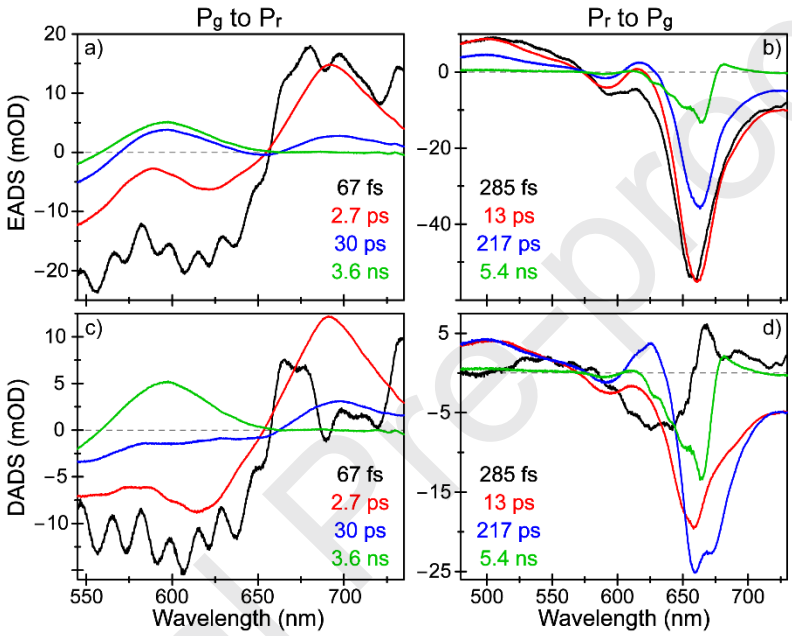

Fig. 3. Global analysis of fs-TA spectra during reversible photoswitching processes of AnPixJg2. The probe window for $P_g \rightarrow P_r$ transition (a, c) was truncated on the blue side (~545 to 735 nm) to remove the residual pump scattering (525 nm) that interferes with analysis. The spectra are ordered from fastest to slowest time constants in black, red, blue, to green with the corresponding lifetimes listed in the inset. For the $P_r \rightarrow P_g$ transition (b, d), the full probe window from ~490 to 735 nm was considered due to the pronounced 664 nm SE band at the red side of the residual pump scattering (650 nm). The EADS (a, b) and DADS (c, d) yield complementary information about the underlying species and reaction kinetics that manifest key spectral changes of the photoexcited PCB cofactor.

Reminiscent of the probe-dependent fits in Fig. 2a-c, the P_g-to-P_r global analysis yields similar time constants of ~70 fs, 2.7 ps, 30 ps, and 3.6 ns (Fig. 3a,c). As the black trace evolves to red, the P_g* ESA, SE, and GSB features become more refined as the wave packet moves out of the Franck-Condon region. The red-to-blue evolution exhibits a pronounced decrease in the initial P_g* species and rise of the ground-state Lumi-G, mainly evinced by the dramatic TA signal sign change below ~650 nm. The rise of the Lumi-G species and recovery of the GSB band corroborate the assignment of the 2.7 ps time constant to the P_g* species moving through a CI (Fig. 4a). The blue-to-green transition with a 30 ps lifetime shows a complete decay of the P_g* ESA band above 650 nm with a slight rise of the Lumi-G absorption band, as well as further recovery of the GSB band below 570 nm. This dynamic component indicates that both the photoreactant P_g and the photoproduct Lumi-G populations are accumulating on a similar time scale after the CI crossing of the P_g* species, again supporting a peaked CI [9,36]. The DADS spectra with less spectral overlap from concurrent species show a cleaner blue trace with no positive band below 650 nm, substantiating the 30 ps relaxation of nascent ground-state species. The longest 3.6 ns time constant is associated with the decay of Lumi-G and a near complete recovery of the GSB, likely involving the chromophore subpopulations that undergo other radiative and nonradiative relaxation pathways [49]. Because our time window is currently limited to 900 ps (see Section 2.4 above), longer time constants are less reliable and are usually averaged in the fs-TA spectral analysis.

As expected, the P_r-to-P_g conversion also exhibits the Franck-Condon relaxation from black to red traces in Fig. 3b,d, involving a notable redshift of the SE band. The red-to-blue transition with a 13 ps lifetime shows further redshift of the P_r* SE band at ~664 nm and blueshift of the ESA band at ~503 nm, suggesting that blue trace remains in the electronic excited state. Accordingly, the intermediate P_r*' band rises (see the blue trace positive band around 620 nm) but decays away

with the 217 ps time constant (Fig. 4b) that likely involves local solvation and surrounding protein residue side chains dynamics [39,41,50,51], while the cofactor accessibility to aqueous phase was demonstrated using the FTIR difference spectrum in H_2O or D_2O medium [20] and the change of solvent accessibility to the cofactor pocket was shown during ns-to-µs molecular dynamics (MD) simulations [41,50]. This short-lived feature substantiates the excited-state population as an intermediate before the CI. The last 5.4 ns component (green trace) shows the residual GSB and fluorescence lifetime (SE decay), while we observed a small positive band around 680 nm (also visible in Fig. 2d above 675 nm at later time points) that is redder than GSB at 648 nm. Therefore, this stage likely has contributions from Lumi-R photoproduct species on the electronic ground state after the C15=C16 bond isomerization (see Fig. 4b), reminiscent of the aforementioned Lumi-G species, albeit with much less transition oscillator strength in the red region [12,20]. Since some of the initial chromophore populations were photoconverted to a new conformer state in our spectroscopic measurements, a long-lived GSB signal is expected for both conversion processes as full recovery occurs on the much longer time scales of microseconds to milliseconds [9,20].

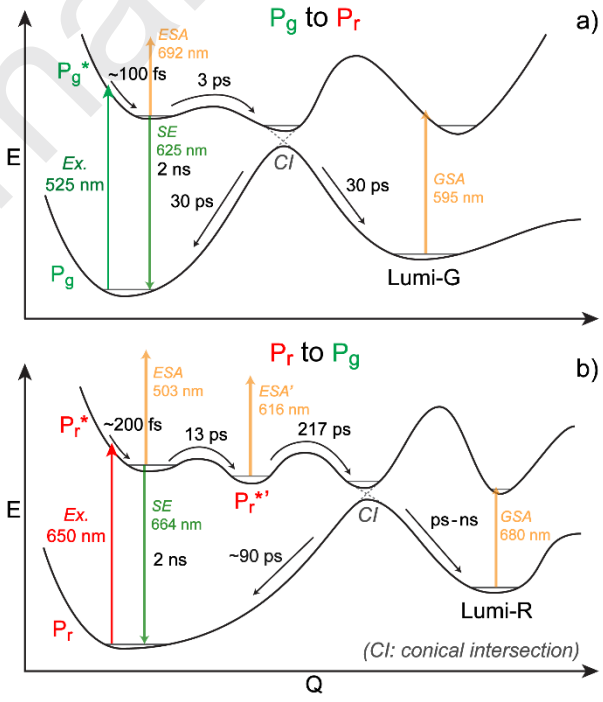

Fig. 4. Potential energy surface for the (a) P_g to P_r and (b) P_r to P_g photoconversion of AnPixJg2. The photoexcitation, ESA, SE, and GSA transitions are represented by vertical arrows with characteristic center wavelengths listed from fs-TA spectra. The arrow length is illustrative and does not exactly scale to the energy gap. Average time constants from the probe-dependent and global analysis are denoted by the curved or tilted arrows connecting reaction species. The nuclear coordinate Q along the D-ring isomerization coordinate is part of a multidimensional landscape that likely involves continuous solvation dynamics and polar residue side-chain motions [39].

Based on TA spectral analysis, we sketch the potential energy surface of the AnPixJg2 PCB cofactor in Fig. 4a and b for the P_g-to-P_r and P_r-to-P_g transitions, respectively. As P_g is excited to P_g* by the 525 nm actinic pump, the initially relaxed P_g* efficiently crosses a small barrier toward the S_1/S_0 CI on the ~3 ps time scale. At the CI, the P_g* population can continue twisting to produce a long-lived Lumi-G species wherein the chromophore resembles P_r, or twist back to repopulate the P_g ground state on a similar time scale of ~30 ps (Figs. 2b,c and 3a,c). On the other hand, the P_r-to-P_g photoconversion exhibits a notably longer excited-state lifetime due to higher transition barriers and the production of a P_r*' intermediate with ~13 ps time constant (Figs. 2e,f and 3b,d). From P_r*', there remains a large barrier to cross before reaching the S_1/S_0 CI to partially produce the Lumi-R species. The P_r* population is shown to be more fluorescent than P_g* (see the larger and longer-lived SE band in Fig. 3b,d than that in Fig. 3a,c) as it was the only species to show some fluorescence before quickly converting to P_g in our spectroscopic experiments. To increase the fluorescence quantum yield for bioimaging applications, an enhancement of the H-bonding network around the D-ring or steric hindrance may help [49] (see Fig. S4 for the chromophore local environment), although it could also decrease the reversible photoswitching quantum yield that may well benefit super-resolution imaging [24,52,53].

3.2. Resonance-enhanced ground-state stimulated Raman spectroscopy

To shed more light on the atomic structures of PCB conformers before and after photoconversion (see Fig. S5 for illustration), we performed GS-FSRS experiments to obtain vibrational signatures of the P_g and P_r species. Given the recent elucidation of local relaxations caused by side chain motions and solvation rather than the structural heterogeneity in a related bacteriophytochrome and CBCR [39,54], we consider FSRS a suitable method to distinguish the solvation dynamics (from excited-state FSRS that tracks the non-equilibrium vibrational dynamics) and structural heterogeneity (from ground-state FSRS that records the equilibrium vibrational features) [28,55,56]. Herein, various Raman pump wavelengths and accompanying broadband Raman probe on the Stokes and anti-Stokes sides were implemented to explore the resonance Raman enhancement effects on the converting species of AnPixJg2 (see Figs. S6 and S7). Overall, the P_g vibrational peaks exhibit a frequency blueshift as compared to the P_r species mainly above 1200 cm^{-1}, in accordance with a more twisted conformation (hence less electronic conjugation across the PCB tetrapyrrole-ring system) in the green-absorbing P_g state [41,43]. To visualize the associated vibrational motions, the density functional theory (DFT)-based Gaussian calculations were performed at B3LYP level with a 6-31G(d,p) basis set (Section 2.5). The calculated Raman spectra show a similar trend to the GS-FSRS data with P_g peaks blue-shifted from P_r peaks (see Fig. 5) mainly in the high-frequency region, with Raman modes above 1600 cm^{-1} tracking the C-D ring and A-B ring methine bridge C=C stretching motions (Table S1) [9,20].

In particular, strong Raman modes at ~1615 and 1649 cm^{-1} in P_r shift to 1630 and 1665 cm^{-1} in P_g, demonstrating the blueshift of 15 and 16 cm^{-1}, respectively. The 1649 and 1665 cm^{-1} modes were assigned to the A-B methine bridge C=C stretch and C–H rocking with A-ring N–H rocking motions (Table S1). The blueshift of this mode from P_r to P_g is due to the A-ring twist (see Fig. S5

and Table S2) that disrupts its H-bonding interactions with the nearby Asp291 and Trp289 (Fig. S4). The main 1615 and 1630 cm^{-1} modes for P_r and P_g species, respectively, involve the C-D methine bridge C=C stretch and C–H rocking with D-ring N-H rocking and C=C stretch. As the D-ring twists more significantly (by ~155°), it most likely breaks the H-bond with Tyr352 and π-π stacking with Trp289, causing the mode frequency blueshift from the ground-state P_r to P_g.

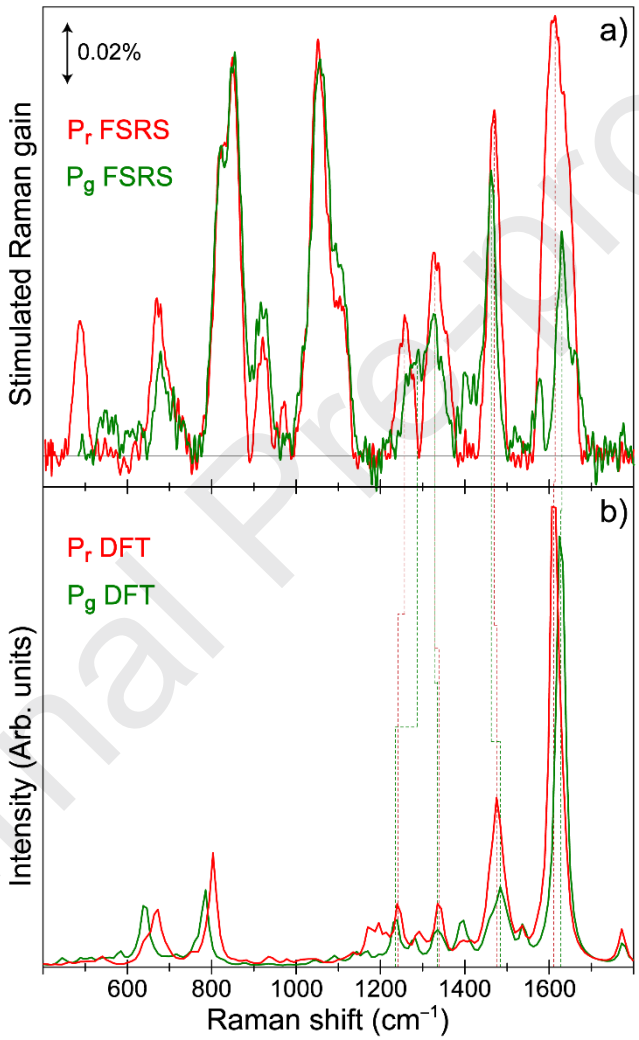

Fig. 5. GS-FSRS of the P_r (red) and P_g (green) conformers of AnPixJg2. The P_r measurement used 505 nm LEDs, 596 nm Raman pump, and Raman probe on the Stokes side. The P_g measurement used 650 nm LEDs, 678 nm Raman pump, and Raman probe on the anti-Stokes side. For the anti-Stokes FSRS spectrum of P_g, the Raman shift and peak intensity axes were multiplied by –1 for

direct comparison with the Stokes FSRS of P_r. Vertical dotted lines depict peak frequency shifts from the experimental to DFT-calculated (frequency scaling factor of 0.97 applied) Raman spectra.

Velazquez Escobar and coworkers previously conducted resonance Raman (RR) of AnPixJg2 using a 1064 nm continuous-wave Raman pump and cooling the sample to −140°C [41] while the red-light-induced photoconversion of AnPixJg2 occurs above −80°C. Raman pump was off-resonance from the P_r and P_g ground-state absorption, and their spectra closely match our calculated Raman spectra (Fig. 5b). The RR spectra also showed a blueshift of the 1630 cm^{-1} mode that was assigned to the C-D methine bridge C=C stretch, with the higher-frequency shoulder assigned to the A-B methine bridge C=C stretch. One of the main differences between the RR at low temperature and GS-FSRS spectra at room temperature lies in two strong bands at ~850 and 1050 cm^{-1} in Fig. 5a, which are also essentially absent in the calculated off-resonance Raman spectra (Fig. 5b). The specific Raman pump used in FSRS could resonantly enhance these specific modes that are vibronically coupled to the electronic transition [29,49,57], since the ~850 and 1050 cm^{-1} modes involve the C-D bridge-H out-of-plane (HOOP) motion [9,13] and D-ring deformations (Table S1), they display significant Huang-Rhys factors and nuclear displacement from the ground to excited state [13,49] and have been observed in previous FSRS measurements of the excited PCB chromophore in Cph1. In particular, the HOOP mode was proposed to be an integral component of the excited-state reaction coordinate toward a C15=C16 isomerized state on the ~3 ps time scale [9], reminiscent of Fig. 4a.

Meanwhile, although the Raman pump wavelength was tuned across the P_r and P_g absorption bands that are separated by over 100 nm, the Raman pump could still photoconvert the sample to a mixed state (Fig. S2) while the LEDs' power was not sufficient for a full conversion to pure

starting species (Fig. 1a). Though an exact match is not expected between the low-temperature off-resonance RR and room-temperature pre-resonance FSRS spectra, we have identified key vibrational signatures of P_r and P_g that support both the D- and A-ring twist after photoconversion (see Fig. S5 for PCB twisting geometries), and resonance conditions that can be further optimized with a strategic combination of tunable Raman pump and probe pulses (Figs. S6 and S7).

Notably, the calculated Raman intensities do not match the experimental values mainly due to the mode-dependent change of resonance conditions using tunable FSRS [29,49,58] and limitation of DFT calculations only focusing on the PCB chromophore here (Fig. S5) without explicit treatment of the protein pocket. In our experiments, various Raman pump wavelengths were used in order to obtain Raman spectrum of a pure P_g or P_r population (e.g., see Fig. S6 for P_g). Surprisingly, each Raman pump resulted in a similar Raman spectrum despite the use of 505 or 650 nm LEDs to generate P_r or P_g species (Fig. S7). To find the cause of this dilemma, the sample was inserted in the actinic pump and Raman pump beam path to see if any photoconversion occurs. Both pumps were able to convert the sample as evinced by a clear color change upon the passage of light. To further investigate the photoconversion of AnPixJg2, we used a fluorimeter arc lamp and a UV/Visible spectrophotometer to excite the sample at different wavelengths and collect the absorption spectra therein (Fig. S2). The finding confirmed that Raman pump overlapping with any ground-state absorption features of AnPixJg2 can induce photoswitching to various extents and cause a mixed population of P_g and P_r. As a result, the 678 nm Raman pump anti-Stokes FSRS with 650 nm LEDs (Fig. 5, green) and 596 nm Raman pump Stokes FSRS with 505 nm LEDs (Fig. 5, red) represent a mixed population with predominant P_g and P_r conformers, respectively. For this reason, AnPixJg2 represents a rather special case that a pre-resonance enhancement condition cannot be directly used to increase the signal-to-noise ratio of a target species [56], because another

species would be readily generated that absorbs more than 100 nm away (see Figs. 1 and S2). Therefore, though the calculations of GS-FSRS spectrum under pre-resonance conditions [59-61] could be helpful to identify key Franck-Condon active modes and yield a better prediction of Raman peak intensities over a broad spectral window (e.g., from low- to high-frequency modes in Fig. 5b), the applicability of such calculations for the P_g and P_r characterization in AnPixJg2 with swift photoswitching remains limited due to key experimental challenges (Figs. S2 and S7) in obtaining the accurate pre-resonance spectrum of pure P_g and P_r species for a rigorous comparison.

Like AnPixJg2, Slr1393g3 is a red/green-photoswitching CBCR with its P_g crystal structure reported (5M82, see Section 2.5) [31], while both CBCRs share the same PCB chromophore with conserved residues around the chromophore (Fig. S4) [19]. The illustrative D and A ring twist between the P_g and P_r conformers may shed some light on the photoswitching process with the D-ring likely twisting on the excited state and A-ring twist on the ground state. This could be due to the change of single- and double-bond character in the excited versus ground state [62,63]. As a conjugated molecule undergoes a π-π^* electronic excitation, a double bond typically adopts more single-bond character, thus allowing it to twist more freely when compared to the ground state. In consequence, after AnPixJg2 is excited, the D-ring twist along the C15=C16 bond constitutes the main reaction coordinate for the cofactor crossing a CI into the ground Lumi state, wherein the A-ring twist along the C5–C6 bond further relaxes the protein on longer time scales with a large-scale conformational change of the surrounding protein pocket and H-bonding network. This reaction stage well beyond the aforementioned ultrafast time scales achieves localization of the π-orbital on PCB in an equilibrated nonplanar conformation of the tetrapyrrole ring system [20] and completes the photoconversion from one absorbing state to another (P_r to P_g, or P_g to P_r). Such a reaction process is also corroborated by local environment of the cofactor chromophore as crystal

structures for phytochromes and CBCRs show less tight packing around the D-ring, so there could be more conformational freedom about the C15 methine bridge than about the C5 or C10 methine bridges (see Figs. 1b and S5 for the atomic numbering of PCB cofactor) [10,11].

3.3. Ground-state heterogeneity and photoconversion quantum yield

The heterogeneity of the ground-state population of CBCRs and phytochromes has brought a vast amount of spectroscopic techniques [12,13,15,64,65] and simulations [40,66] to determine how many subpopulations each species has as well as how their dynamics differ. The heterogeneity in phytochromes and CBCRs points toward a common feature that could be linked to a functional role in nature or evolution advantage. As for AnPixJg2 in solution, Scarbath-Evers et al. implemented MD simulations on a 1 μs time scale in correlation with experimental ^{13}C cross-polarization magic-angle spinning NMR spectroscopy that uncovered two sub-states in P_r where the D-ring adopts two different isomers [50]. This finding is also in line with Kim et al. reporting their TA and global analysis data on a similar red/green CBCR, NpR6012g4, tracking two $^{15Z}P_r$ subpopulations that photoconvert to ^{15E}Lumi-R species on separate time scales of ~75 ps and 1 ns [15]. On the other hand, Rao and coworkers recently published QM/MM calculations on AnPixJg2 where the D-ring heterogeneity could be mainly governed by the protonation states of histidine residues around the chromophore [40]. Therefore, we surmise that the highly overlapped TA spectra observed during the P_r-to-P_g photoconversion of AnPixJg2 (Fig. 2d) are likely due to a heterogeneous ground-state population that produces Lumi-R on the hundreds of ps to few ns time scales (Figs. 2f and 3b). Different subpopulations in P_r could also be the cause of the ground-state shoulder peak at ~592 nm (Fig. 1a) and the resulting GSB band (Fig. 2d), as well as the mismatch between the apparent time constants and the retrieved time constants from global analysis on the

basis of a homogeneous model for dominant species (Fig. 4b). Based on the current GS-FSRS data of the P_g and P_r species of AnPixJg2 with a series of Raman pump, Raman probe, and LED wavelengths (Fig. S7), the Raman peak widths are similar across a spectral window over ~1100 cm^{-1} for both P_g and P_r species, which suggests that the structural heterogeneity remain largely unchanged before and after the reversible photoswitching events.

Looking forward, an actinic-pump-dependent TA and FSRS experiment with tunable Raman pump wavelengths would help to uncover the number of ground-state subpopulations and their photoconversion dynamics [13,39]. Moreover, the time-resolved excited-state FSRS will be implemented in future studies on the PCB cofactor along with a newly engineered AnPixJg2_BV4 with just four mutated residues in the protein pocket (e.g., Fig. S4 that plays a critical role on the ultrafast photochemistry and function of the photosensory unit) which can bind the BV cofactor (see Section 2.1) for mammalian cell applications [21]. Preliminary TA results of AnPixJg2_BV4 (PCB) in our lab showed altered time constants on the ps-to-ns time scales and a more homogeneous population in the P_r state due to a less restrictive and more flexible chromophore pocket (versus AnPixJg2), which will be reported in a subsequent publication. In particular, similar pre-resonance and off-resonance conditions (as in Figs. S6 and S7) will be implemented for AnPixJg2_BV4 (PCB) to directly compare with AnPixJg2 (PCB) to gain further insights into the correlation between structural heterogeneity and Raman peak width, aided by the excited-state dynamics of Raman peaks that could report on local relaxation at the active site as well as subpopulations of the chromophore (hence enabling an evaluation of the dominant factor) [24,56].

The photoconversion quantum yield for AnPixJg2 has yet to be reported, but based on the phylogenetically related NpR6012g4, the P_r-to-P_g photoconversion should be close to 40% [15], consistent with the CI-branching and generation of various ground-state intermediates depicted in

Fig. 4b. The rather efficient photoconversion (more than canonical phytochromes at <15% [9,12]) was observed upon irradiating the sample with multiple types of light (vide supra). Previous TA work on a four-ring molecular photoswitch (1,2-dithienyl-1,2-dicyanoethene, 4TCE) showed that the GSB recovery dynamics on the 40 ps time scale could be used to obtain the trans-to-cis isomerization yield [67]. However, this approach is much less applicable for AnPixJg2 due to a significant overlap between transient GSB and GSA bands (Fig. 2a) or GSB and ESA bands (Fig. 2d), the significantly larger isomerization time constant (Fig. 4b), as well as the lack of direct observation of the final photoproducts P_r and P_g beyond Lumi-G and Lumi-R in Fig. 4a and b, respectively, within our experimental time window of 600–900 ps (Fig. 2). Furthermore, the ps narrowband Raman pump pulse can cause the sample to photoconvert, making it rather challenging to find an optimal resonance condition that would enhance the P_r and P_g species separately (see Fig. S7). All excitations, even at 800 nm center wavelength, can convert AnPixJg2 from the native state to a different mixed population state (Fig. S2), thus prompting us to further select a suitable combination of LEDs, Raman pump, and Raman probe to collect reliable GS-FSRS spectrum of a specific conformer (e.g., P_g in Fig. S6, and P_r in Fig. 5) with key vibrational signatures.

Comparing the ultrafast photoconversion processes revealed in this work to previously studied phytochromes and CBCRs [9,15,16], a common trend emerges where the forward reaction exhibits a longer-lived excited state as it moves from a stable conformer to a meta-stable conformer. In particular, both the ground- and excited-state energetics need to be considered to map out the potential energy landscape for photoconversion. The longer-lived excited state naturally corresponds to more complex relaxation pathways before it produces the photointermediate or Lumi-R state (e.g., Fig. 4b). With the reverse photoconversion, moving away from a meta-stable conformer with less chromophore tetrapyrrole-ring π-conjugation [43] helps the system to relax

across a smaller barrier en route to the Lumi intermediate. The TA-uncovered major lifetimes of ~3 and 30 ps for P_g* species (Fig. 4a) and ~13 and 217 ps for P_r* species (Fig. 4b) are congruent with the primary decay time constants of fluorescence at 42 ps and 200 ps for APg_{543}* (same as P_g*, emission peak at 610 nm) and APr_{648}* (same as P_r*, emission peak at 670 nm), respectively [20]. In both cases, the excited-state reaction barriers naturally involve the D-ring flipping motions, concomitant with ultrafast motions of the surrounding solvent molecules and residue side chains that underlie the chromophore-protein interactions in real time [54,56].

4. Conclusions

In summary, we have performed the wavelength-tunable fs-TA and GS-FSRS studies of both the forward ($^{15Z}P_r$ to $^{15E}P_g$) and reverse ($^{15E}P_g$ to $^{15Z}P_r$) photoconversion of a CBCR AnPixJg2 in buffer solution at room temperature, essentially tracking the protein-chromophore interactions on intrinsic molecular time scales. The forward reaction exhibits a longer-lived excited state and requires two distinct steps with ~13 and 217 ps time constants before reaching the CI to form the photoproduct (Lumi-R). Conversely, the reverse reaction exhibits a much faster excited-state decay and takes a dominant ~3 ps step to cross a small barrier to reach the CI, allowing us to resolve the Lumi-G accumulation on the 30 ps time scale within our detection time window. The primary photochemical reaction coordinate has been attributed to a facile C15=C16 bond isomerization that occurs on ultrafast time scales inside a tightly packed yet highly dynamic chromophore pocket, which supports photoconversion via S_1/S_0 CIs.

Besides gaining fundamental insights into the reversible photoswitching processes of PCB cofactor in AnPixJg2 upon electronic excitation, we have also provided vibrational signatures of the red-absorbing ground state versus green-absorbing photoproduct via resonance Raman enhancement across the visible to near-IR region. A strategic combination of the continuous-wave

LEDs, ps Raman pump wavelengths, and fs Raman probe on the Stokes or anti-Stokes side allows us to reveal a common blueshift of the high-frequency Raman modes from the P_r to P_g species, corroborated by quantum chemistry calculations of the respective ground-state chromophore structure involving a major D-ring twist and minor A-ring twist between the P_r and P_g conformers. We envision that the deciphered mechanistic information at molecular level with correlated electronic and vibrational signatures on ultrafast time scales can enable the targeted design of photosensory units in protein matrix from the bottom up, achieving desirable properties in imaging and optogenetic applications from color tuning, brightness, stability, to photoswitching efficiency, reversibility, and signal contrast in more realistic environments.

CRediT authorship contribution statement

S.R. Tachibana: Conceptualization, Investigation, Formal analysis, Data curation, Writing – original draft. **L. Tang:** Investigation, Formal analysis, Methodology, Visualization, Writing – review & editing. **C. Chen:** Investigation, Validation, Writing – review & editing. **L. Zhu:** Investigation, Methodology. **Y. Takeda:** Methodology, Writing – review & editing. **K. Fushimi:** Methodology, Writing – review & editing. **T.K. Seevers:** Formal analysis, Validation. **R. Narikawa:** Conceptualization, Resources, Funding acquisition, Investigation, Methodology, Writing – review & editing. **M. Sato:** Conceptualization, Resources, Funding acquisition, Methodology. **C. Fang:** Conceptualization, Investigation, Methodology, Resources, Funding acquisition, Supervision, Data curation, Writing – review & editing.

Declaration of competing interest

The authors declare that they have no known competing financial interests or personal relationships that could have appeared to influence the work reported in this paper.

Acknowledgements

This work was supported by the U.S. National Science Foundation (NSF, grant number MCB-1817949) to C.F. Additional personnel support was provided by the NSF MRI development grant (DMR-1920368). This work was partly supported by grants from JST, CREST (JPMJCR1653 to M.S. and R.N.). C.C. appreciates the Oregon State University Department of Chemistry Graduate Research Fellowship in Summer 2020.

Appendix A. Supplementary data

Supplementary data to this article can be found online at https://doi.org/10.1016/j.saa.2020.XXXXXX.

References

[1] M. Ikeuchi, T. Ishizuka, Cyanobacteriochromes: a new superfamily of tetrapyrrole-binding photoreceptors in cyanobacteria, Photochem. Photobiol. Sci. 7 (2008) 1159-1167. https://doi.org/10.1039/B802660M.

[2] X. Shu, A. Royant, M.Z. Lin, T.A. Aguilera, V. Lev-Ram, P.A. Steinbach, R.Y. Tsien, Mammalian expression of infrared fluorescent proteins engineered from a bacterial phytochrome, Science 324 (2009) 804-807. https://doi.org/10.1126/science.1168683.

[3] G.S. Filonov, K.D. Piatkevich, L.-M. Ting, J. Zhang, K. Kim, V.V. Verkhusha, Bright and stable near-infrared fluorescent protein for in vivo imaging, Nat. Biotechnol. 29 (2011) 757-761. https://doi.org/10.1038/nbt.1918.

[4] K.D. Piatkevich, F.V. Subach, V.V. Verkhusha, Engineering of bacterial phytochromes for near-infrared imaging, sensing, and light-control in mammals, Chem. Soc. Rev. 42 (2013) 3441-3452. https://doi.org/10.1039/C3CS35458J.

[5] N.C. Rockwell, Y.-S. Su, J.C. Lagarias, Phytochrome structure and signaling mechanisms, Annu. Rev. Plant Biol. 57 (2006) 837-858. https://doi.org/10.1146/annurev.arplant.56.032604.144208.

[6] M.-H. Ryu, M. Gomelsky, Near-infrared light responsive synthetic c-di-GMP module for optogenetic applications, ACS Synth. Biol. 3 (2014) 802-810. https://doi.org/10.1021/sb400182x.

[7] F. Pennacchietti, A. Losi, X.-l. Xu, K.-h. Zhao, W. Gärtner, C. Viappiani, F. Cella, A. Diaspro, S. Abbruzzetti, Photochromic conversion in a red/green cyanobacteriochrome from Synechocystis PCC6803: quantum yields in solution and photoswitching dynamics in living E. coli cells, Photochem. Photobiol. Sci. 14 (2015) 229-237. https://doi.org/10.1039/C4PP00337C.

[8] K. Fushimi, G. Enomoto, M. Ikeuchi, R. Narikawa, Distinctive properties of dark reversion kinetics between two red/green-type cyanobacteriochromes and their application in the photoregulation of cAMP synthesis, Photochem. Photobiol. 93 (2017) 681-691. https://doi.org/10.1111/php.12732.

[9] J. Dasgupta, R.R. Frontiera, K.C. Taylor, J.C. Lagarias, R.A. Mathies, Ultrafast excited-state isomerization in phytochrome revealed by femtosecond stimulated Raman spectroscopy, Proc. Natl. Acad. Sci. U. S. A. 106 (2009) 1784-1789. https://doi.org/10.1073/pnas.0812056106.

[10] N.C. Rockwell, J.C. Lagarias, A brief history of phytochromes, ChemPhysChem 11 (2010) 1172-1180. https://doi.org/10.1002/cphc.200900894.

[11] K. Fushimi, R. Narikawa, Cyanobacteriochromes: photoreceptors covering the entire UV-to-visible spectrum, Curr. Opin. Struct. Biol. 57 (2019) 39-46. https://doi.org/https://doi.org/10.1016/j.sbi.2019.01.018.

[12] P.W. Kim, L.H. Freer, N.C. Rockwell, S.S. Martin, J.C. Lagarias, D.S. Larsen, Second-chance forward isomerization dynamics of the red/green cyanobacteriochrome NpR6012g4 from Nostoc punctiforme, J. Am. Chem. Soc. 134 (2012) 130-133. https://doi.org/10.1021/ja209533x.

[13] K.M. Spillane, J. Dasgupta, J.C. Lagarias, R.A. Mathies, Homogeneity of phytochrome Cph1 vibronic absorption revealed by resonance Raman intensity analysis, J. Am. Chem. Soc. 131 (2009) 13946-13948. https://doi.org/10.1021/ja905822m.

[14] Y. Yang, K. Heyne, R.A. Mathies, J. Dasgupta, Non-bonded interactions drive the sub-picosecond bilin photoisomerization in the Pfr state of phytochrome Cph1, ChemPhysChem 17 (2016) 369-374. https://doi.org/10.1002/cphc.201501073.

[15] P.W. Kim, L.H. Freer, N.C. Rockwell, S.S. Martin, J.C. Lagarias, D.S. Larsen, Femtosecond photodynamics of the red/green cyanobacteriochrome NpR6012g4 from Nostoc punctiforme. 1. Forward dynamics, Biochemistry 51 (2012) 608-618. https://doi.org/10.1021/bi201507k.

[16] P.W. Kim, L.H. Freer, N.C. Rockwell, S.S. Martin, J.C. Lagarias, D.S. Larsen, Femtosecond photodynamics of the red/green cyanobacteriochrome NpR6012g4 from Nostoc punctiforme. 2. Reverse dynamics, Biochemistry 51 (2012) 619-630. https://doi.org/10.1021/bi2017365.

[17] C. Song, R. Narikawa, M. Ikeuchi, W. Gärtner, J. Matysik, Color tuning in red/green cyanobacteriochrome AnPixJ: photoisomerization at C15 causes an excited-state destabilization, J. Phys. Chem. B 119 (2015) 9688-9695. https://doi.org/10.1021/acs.jpcb.5b04655.

[18] R. Narikawa, Y. Fukushima, T. Ishizuka, S. Itoh, M. Ikeuchi, A novel photoactive GAF domain of cyanobacteriochrome AnPixJ that shows reversible green/red photoconversion, J. Mol. Biol. 380 (2008) 844-855. https://doi.org/https://doi.org/10.1016/j.jmb.2008.05.035.

[19] R. Narikawa, T. Ishizuka, N. Muraki, T. Shiba, G. Kurisu, M. Ikeuchi, Structures of cyanobacteriochromes from phototaxis regulators AnPixJ and TePixJ reveal general and specific photoconversion mechanism, Proc. Natl. Acad. Sci. U. S. A. 110 (2013) 918-923. https://doi.org/10.1073/pnas.1212098110.

[20] Y. Fukushima, M. Iwaki, R. Narikawa, M. Ikeuchi, Y. Tomita, S. Itoh, Photoconversion mechanism of a green/red photosensory cyanobacteriochrome AnPixJ: time-resolved optical spectroscopy and FTIR analysis of the AnPixJ-GAF2 domain, Biochemistry 50 (2011) 6328-6339. https://doi.org/10.1021/bi101799w.

[21] K. Fushimi, T. Miyazaki, Y. Kuwasaki, T. Nakajima, T. Yamamoto, K. Suzuki, Y. Ueda, K. Miyake, Y. Takeda, J.-H. Choi, H. Kawagishi, E.Y. Park, M. Ikeuchi, M. Sato, R. Narikawa, Rational conversion of chromophore selectivity of cyanobacteriochromes to accept mammalian intrinsic biliverdin, Proc. Natl. Acad. Sci. U. S. A. 116 (2019) 8301-8309. https://doi.org/10.1073/pnas.1818836116.

[22] K. Mukougawa, H. Kanamoto, T. Kobayashi, A. Yokota, T. Kohchi, Metabolic engineering to produce phytochromes with phytochromobilin, phycocyanobilin, or phycoerythrobilin chromophore in Escherichia coli, FEBS Lett. 580 (2006) 1333-1338. https://doi.org/https://doi.org/10.1016/j.febslet.2006.01.051.

[23] K. Miyake, K. Fushimi, T. Kashimoto, K. Maeda, W. Ni Ni, H. Kimura, M. Sugishima, M. Ikeuchi, R. Narikawa, Functional diversification of two bilin reductases for light perception

and harvesting in unique cyanobacterium Acaryochloris marina MBIC 11017, FEBS J. 287 (2020) 4016-4031. https://doi.org/10.1111/febs.15230.

[24] T.D. Krueger, L. Tang, L. Zhu, I.L. Breen, R.M. Wachter, C. Fang, Dual illumination enhances transformation of an engineered green-to-red photoconvertible fluorescent protein, Angew. Chem. Int. Ed. 59 (2020) 1644-1652. https://doi.org/10.1002/anie.201911379.

[25] W. Liu, Y. Wang, L. Tang, B.G. Oscar, L. Zhu, C. Fang, Panoramic portrait of primary molecular events preceding excited state proton transfer in water, Chem. Sci. 7 (2016) 5484-5494. https://doi.org/10.1039/C6SC00672H.

[26] L. Tang, L. Zhu, M.A. Taylor, Y. Wang, S.J. Remington, C. Fang, Excited state structural evolution of a GFP single-site mutant tracked by tunable femtosecond-stimulated Raman spectroscopy, Molecules 23 (2018) 2226. https://doi.org/10.3390/molecules23092226.

[27] L. Zhu, W. Liu, C. Fang, A versatile femtosecond stimulated Raman spectroscopy setup with tunable pulses in the visible to near infrared, Appl. Phys. Lett. 105 (2014) 041106. https://doi.org/10.1063/1.4891766.

[28] C. Fang, L. Tang, B.G. Oscar, C. Chen, Capturing structural snapshots during photochemical reactions with ultrafast Raman spectroscopy: from materials transformation to biosensor responses, J. Phys. Chem. Lett. 9 (2018) 3253–3263. https://doi.org/10.1021/acs.jpclett.8b00373.

[29] K. Roy, S. Kayal, F. Ariese, A. Beeby, S. Umapathy, Mode specific excited state dynamics study of bis(phenylethynyl)benzene from ultrafast Raman loss spectroscopy, J. Chem. Phys. 146 (2017) 064303. https://doi.org/10.1063/1.4975174.

[30] M.J. Frisch, G.W. Trucks, H.B. Schlegel, G.E. Scuseria, M.A. Robb, J.R. Cheeseman, G. Scalmani, V. Barone, G.A. Petersson, H. Nakatsuji, X. Li, M. Caricato, A.V. Marenich, J.

Bloino, B.G. Janesko, R. Gomperts, B. Mennucci, H.P. Hratchian, J.V. Ortiz, A.F. Izmaylov, J.L. Sonnenberg, D. Williams-Young, F. Ding, F. Lipparini, F. Egidi, J. Goings, B. Peng, A. Petrone, T. Henderson, D. Ranasinghe, V.G. Zakrzewski, J. Gao, N. Rega, G. Zheng, W. Liang, M. Hada, M. Ehara, K. Toyota, R. Fukuda, J. Hasegawa, M. Ishida, T. Nakajima, Y. Honda, O. Kitao, H. Nakai, T. Vreven, K. Throssell, J. J. A. Montgomery, J.E. Peralta, F. Ogliaro, M.J. Bearpark, J.J. Heyd, E.N. Brothers, K.N. Kudin, V.N. Staroverov, T.A. Keith, R. Kobayashi, J. Normand, K. Raghavachari, A.P. Rendell, J.C. Burant, S.S. Iyengar, J. Tomasi, M. Cossi, J.M. Millam, M. Klene, C. Adamo, R. Cammi, J.W. Ochterski, R.L. Martin, K. Morokuma, O. Farkas, J.B. Foresman, D.J. Fox, Gaussian 16, Revision A.03, in, Gaussian, Inc., Wallingford, CT, 2016.

[31] X. Xu, A. Höppner, C. Wiebeler, K.-H. Zhao, I. Schapiro, W. Gärtner, Structural elements regulating the photochromicity in a cyanobacteriochrome, Proc. Natl. Acad. Sci. U. S. A. 117 (2020) 2432-2440. https://doi.org/10.1073/pnas.1910208117.

[32] X.-L. Xu, A. Gutt, J. Mechelke, S. Raffelberg, K. Tang, D. Miao, L. Valle, C.D. Borsarelli, K.-H. Zhao, W. Gärtner, Combined mutagenesis and kinetics characterization of the bilin-binding GAF domain of the protein Slr1393 from the cyanobacterium Synechocystis PCC6803, ChemBioChem 15 (2014) 1190-1199. https://doi.org/10.1002/cbic.201400053.

[33] A.P. Scott, L. Radom, Harmonic vibrational frequencies: an evaluation of Hartree−Fock, Møller−Plesset, quadratic configuration interaction, density functional theory, and semiempirical scale factors, J. Phys. Chem. 100 (1996) 16502-16513. https://doi.org/10.1021/jp960976r.

[34] J.P. Merrick, D. Moran, L. Radom, An evaluation of harmonic vibrational frequency scale factors, J. Phys. Chem. A 111 (2007) 11683-11700. https://doi.org/10.1021/jp073974n.

[35] W. Liu, F. Han, C. Smith, C. Fang, Ultrafast conformational dynamics of pyranine during excited state proton transfer in aqueous solution revealed by femtosecond stimulated Raman spectroscopy, J. Phys. Chem. B 116 (2012) 10535-10550. https://doi.org/10.1021/jp3020707.

[36] T. Kumpulainen, B. Lang, A. Rosspeintner, E. Vauthey, Ultrafast elementary photochemical processes of organic molecules in liquid solution, Chem. Rev. 117 (2017) 10826-10939. https://doi.org/10.1021/acs.chemrev.6b00491.

[37] M.A. Taylor, L. Zhu, N.D. Rozanov, K.T. Stout, C. Chen, C. Fang, Delayed vibrational modulation of the solvated GFP chromophore into a conical intersection, Phys. Chem. Chem. Phys. 21 (2019) 9728-9739. https://doi.org/10.1039/C9CP01077G.

[38] L. Tang, C. Fang, Nitration of tyrosine channels photoenergy through a conical intersection in water, J. Phys. Chem. B 123 (2019) 4915-4928. https://doi.org/10.1021/acs.jpcb.9b03464.

[39] D. Wang, X. Li, S. Zhang, L. Wang, X. Yang, D. Zhong, Revealing the origin of multiphasic dynamic behaviors in cyanobacteriochrome, Proc. Natl. Acad. Sci. U. S. A. 117 (2020) 19731-19736. https://doi.org/10.1073/pnas.2001114117.

[40] A.G. Rao, C. Wiebeler, S. Sen, D.S. Cerutti, I. Schapiro, Histidine protonation controls structural heterogeneity in the cyanobacteriochrome AnPixJg2, bioRxiv (2020) 2020.2008.2021.260158. https://doi.org/10.1101/2020.08.21.260158.

[41] F. Velazquez Escobar, T. Utesch, R. Narikawa, M. Ikeuchi, M.A. Mroginski, W. Gärtner, P. Hildebrandt, Photoconversion mechanism of the second GAF domain of cyanobacteriochrome AnPixJ and the cofactor structure of its green-absorbing state, Biochemistry 52 (2013) 4871-4880. https://doi.org/10.1021/bi400506a.

[42] N.C. Rockwell, S.S. Martin, S. Lim, J.C. Lagarias, J.B. Ames, Characterization of red/green cyanobacteriochrome NpR6012g4 by solution nuclear magnetic resonance spectroscopy: a

protonated bilin ring system in both photostates, Biochemistry 54 (2015) 2581-2600. https://doi.org/10.1021/bi501548t.

[43] C. Wiebeler, A.G. Rao, W. Gärtner, I. Schapiro, The effective conjugation length is responsible for the red/green spectral tuning in the cyanobacteriochrome Slr1393g3, Angew. Chem. Int. Ed. 58 (2019) 1934-1938. https://doi.org/10.1002/anie.201810266.

[44] I.H.M. van Stokkum, D.S. Larsen, R. van Grondelle, Global and target analysis of time-resolved spectra, Biochim. Biophys. Acta 1657 (2004) 82-104. https://doi.org/http://doi.org/10.1016/j.bbabio.2004.04.011.

[45] J.J. Snellenburg, S.P. Laptenok, R. Seger, K.M. Mullen, I.H.M. van Stokkum, Glotaran: a Java-based graphical user interface for the R-package TIMP, J. Stat. Softw. 49 (2012) 1-22. https://doi.org/10.18637/jss.v049.i03.

[46] A.R. Holzwarth, Chapter 5: Data Analysis of Time-Resolved Measurements, in: J. Amesz, A.J. Hoff (Eds.) Biophysical Techniques in Photosynthesis, Kluwer Academic Publishers; Springer, Dordrecht, Netherlands, 1996, pp. 75-92.

[47] K.C. Toh, E.A. Stojkovic, I.H.M. van Stokkum, K. Moffat, J.T.M. Kennis, Proton-transfer and hydrogen-bond interactions determine fluorescence quantum yield and photochemical efficiency of bacteriophytochrome, Proc. Natl. Acad. Sci. U. S. A. 107 (2010) 9170-9175. https://doi.org/10.1073/pnas.0911535107.

[48] C. Chen, L. Zhu, S.A. Boulanger, N.S. Baleeva, I.N. Myasnyanko, M.S. Baranov, C. Fang, Ultrafast excited-state proton transfer dynamics in dihalogenated non-fluorescent and fluorescent GFP chromophores, J. Chem. Phys. 152 (2020) 021101. https://doi.org/10.1063/1.5138666.

[49] C. Fang, L. Tang, C. Chen, Unveiling coupled electronic and vibrational motions of chromophores in condensed phases, J. Chem. Phys. 151 (2019) 200901. https://doi.org/10.1063/1.5128388.

[50] L.K. Scarbath-Evers, S. Jähnigen, H. Elgabarty, C. Song, R. Narikawa, J. Matysik, D. Sebastiani, Structural heterogeneity in a parent ground-state structure of AnPixJg2 revealed by theory and spectroscopy, Phys. Chem. Chem. Phys. 19 (2017) 13882-13894. https://doi.org/10.1039/C7CP01218G.

[51] E. Claesson, W.Y. Wahlgren, H. Takala, S. Pandey, L. Castillon, V. Kuznetsova, L. Henry, M. Panman, M. Carrillo, J. Kübel, R. Nanekar, L. Isaksson, A. Nimmrich, A. Cellini, D. Morozov, M. Maj, M. Kurttila, R. Bosman, E. Nango, R. Tanaka, T. Tanaka, L. Fangjia, S. Iwata, S. Owada, K. Moffat, G. Groenhof, E.A. Stojković, J.A. Ihalainen, M. Schmidt, S. Westenhoff, The primary structural photoresponse of phytochrome proteins captured by a femtosecond X-ray laser, eLife 9 (2020) e53514. https://doi.org/10.7554/eLife.53514.

[52] D. Bourgeois, V. Adam, Reversible photoswitching in fluorescent proteins: a mechanistic view, IUBMB Life 64 (2012) 482-491. https://doi.org/10.1002/iub.1023.

[53] K. Nienhaus, G.U. Nienhaus, Fluorescent proteins for live-cell imaging with super-resolution, Chem. Soc. Rev. 43 (2014) 1088-1106. https://doi.org/10.1039/C3CS60171D.

[54] D. Wang, Y. Qin, M. Zhang, X. Li, L. Wang, X. Yang, D. Zhong, The origin of ultrafast multiphasic dynamics in photoisomerization of bacteriophytochrome, J. Phys. Chem. Lett. 11 (2020) 5913-5919. https://doi.org/10.1021/acs.jpclett.0c01394.

[55] C. Fang, R.R. Frontiera, R. Tran, R.A. Mathies, Mapping GFP structure evolution during proton transfer with femtosecond Raman spectroscopy, Nature 462 (2009) 200-204. https://doi.org/10.1038/nature08527.

[56] C. Fang, L. Tang, Mapping structural dynamics of proteins with femtosecond stimulated Raman spectroscopy, Annu. Rev. Phys. Chem. 71 (2020) 239-265. https://doi.org/10.1146/annurev-physchem-071119-040154.

[57] B.G. Oscar, C. Chen, W. Liu, L. Zhu, C. Fang, Dynamic Raman line shapes on an evolving excited-state landscape: insights from tunable femtosecond stimulated Raman spectroscopy, J. Phys. Chem. A 121 (2017) 5428-5441. https://doi.org/10.1021/acs.jpca.7b04404.

[58] C. Chen, L. Zhu, C. Fang, Femtosecond stimulated Raman line shapes: dependence on resonance conditions of pump and probe pulses, Chin. J. Chem. Phys. 31 (2018) 492-502. https://doi.org/10.1063/1674-0068/31/cjcp1805125.

[59] A.B. Myers, R.A. Mathies, Resonance Raman Intensities: A Probe of Excited-State Structure and Dynamics, in: T.G. Spiro (Ed.) Biological Applications of Raman Spectroscopy, John Wiley & Sons, Inc., New York, 1987, pp. 1-58.

[60] M.S. Barclay, T.J. Quincy, D.B. Williams-Young, M. Caricato, C.G. Elles, Accurate assignments of excited-state resonance Raman spectra: a benchmark study combining experiment and theory, J. Phys. Chem. A 121 (2017) 7937-7946. https://doi.org/10.1021/acs.jpca.7b09467.

[61] P.C. Andrikopoulos, Y. Liu, A. Picchiotti, N. Lenngren, M. Kloz, A.S. Chaudhari, M. Precek, M. Rebarz, J. Andreasson, J. Hajdu, B. Schneider, G. Fuertes, Femtosecond-to-nanosecond dynamics of flavin mononucleotide monitored by stimulated Raman spectroscopy and simulations, Phys. Chem. Chem. Phys. 22 (2020) 6538-6552. https://doi.org/10.1039/C9CP04918E.

[62] C.A. Guido, D. Jacquemin, C. Adamo, B. Mennucci, On the TD-DFT accuracy in determining single and double bonds in excited-state structures of organic molecules, J. Phys. Chem. A 114 (2010) 13402-13410. https://doi.org/10.1021/jp109218z.

[63] I.V. Polyakov, B.L. Grigorenko, E.M. Epifanovsky, A.I. Krylov, A.V. Nemukhin, Potential energy landscape of the electronic states of the GFP chromophore in different protonation forms: electronic transition energies and conical intersections, J. Chem. Theory Comput. 6 (2010) 2377-2387. https://doi.org/10.1021/ct100227k.

[64] C. Song, G. Psakis, C. Lang, J. Mailliet, W. Gärtner, J. Hughes, J. Matysik, Two ground state isoforms and a chromophore D-ring photoflip triggering extensive intramolecular changes in a canonical phytochrome, Proc. Natl. Acad. Sci. U. S. A. 108 (2011) 3842-3847. https://doi.org/10.1073/pnas.1013377108.

[65] P.W. Kim, N.C. Rockwell, S.S. Martin, J.C. Lagarias, D.S. Larsen, Heterogeneous photodynamics of the P_{fr} State in the cyanobacterial phytochrome Cph1, Biochemistry 53 (2014) 4601-4611. https://doi.org/10.1021/bi5005359.

[66] S. Kaminski, G. Daminelli, M.A. Mroginski, Molecular dynamics simulations of the chromophore binding site of Deinococcus radiodurans bacteriophytochrome using new force field parameters for the phytochromobilin chromophore, J. Phys. Chem. B 113 (2009) 945-958. https://doi.org/10.1021/jp8047532.

[67] J. Zhou, X. Guo, H.E. Katz, A.E. Bragg, Molecular switching via multiplicity-exclusive E/Z photoisomerization pathways, J. Am. Chem. Soc. 137 (2015) 10841-10850. https://doi.org/10.1021/jacs.5b07348.

Graphical Abstract

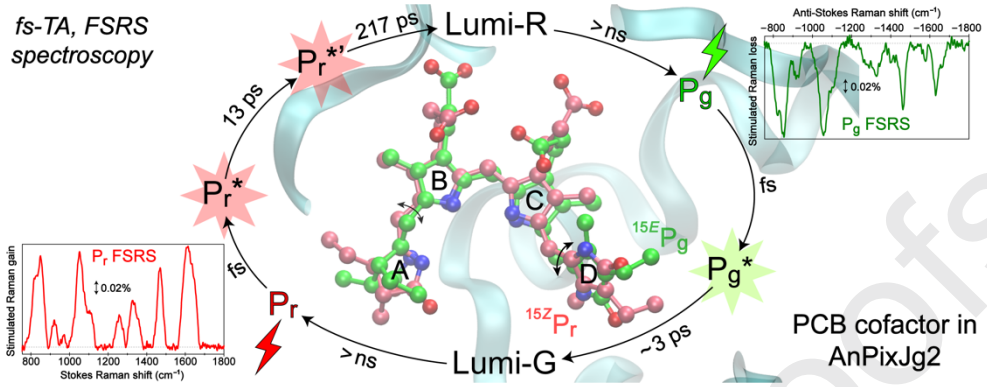

Highlights

- Cyanobacteriochromes display effective and efficient red/green photoswitching behavior
- Femtosecond transient absorption spectroscopy revealed distinct intermediates
- Forward (red-to-green) is slower than reverse (green-to-red) reaction of AnPixJg2
- Tunable femtosecond stimulated Raman spectroscopy (FSRS) tracks protein color change
- Excited PCB cofactor undergoes ultrafast internal conversion to the ground state

CRediT authorship contribution statement

S.R. Tachibana: Conceptualization, Investigation, Formal analysis, Data curation, Writing – original draft. **L. Tang:** Investigation, Formal analysis, Methodology, Visualization, Writing – review & editing. **C. Chen:** Investigation, Validation, Writing – review & editing. **L. Zhu:** Investigation, Methodology. **Y. Takeda:** Methodology, Writing – review & editing. **K. Fushimi:** Methodology, Writing – review & editing. **T.K. Seevers:** Formal analysis, Validation. **R. Narikawa:** Conceptualization, Resources, Funding acquisition, Investigation, Methodology,

Writing – review & editing. **M. Sato:** Conceptualization, Resources, Funding acquisition, Methodology. **C. Fang:** Conceptualization, Investigation, Methodology, Resources, Funding acquisition, Supervision, Data curation, Writing – review & editing.

Declaration of interests

☒ The authors declare that they have no known competing financial interests or personal relationships that could have appeared to influence the work reported in this paper.

☐ The authors declare the following financial interests/personal relationships which may be considered as potential competing interests: